Original Article

Numerical simulation on sand sedimentation and erosion characteristics around HDPE sheet sand barrier under different wind angles

ZHANG Kai[1,2] https://orcid.org/0000-0002-4760-8860; e-mail: zhangkai0212@yeah.net

ZHANG Peili[1] https://orcid.org/0009-0001-6650-3677; e-mail: 874058528@qq.com

ZHANG Hailong[1] https://orcid.org/0000-0003-2499-505X; e-mail: 1138804643@qq.com

TIAN Jianjin[1] https://orcid.org/0009-0006-3168-1701; e-mail: Tjj19991202@yeah.net

WANG Zhenghui[1] https://orcid.org/0000-0002-0642-8038; e-mail: wangzh2234@163.com

XIAO Jianhua[3*] https://orcid.org/0000-0002-5899-9502; ✉ e-mail: xiaojh@lzb.ac.cn

*Corresponding author

1 College of Civil Engineering, Lanzhou Jiaotong University, Lanzhou 730000, China

2 Key Laboratory of Desert and Desertification, Northwest Institute of Eco-Environment and Resources, Chinese Academy of Sciences, Lanzhou 730000, China

3 Key Laboratory of Ecological Safety and Sustainable Development in Arid Lands, Northwest Institute of Eco-Environment and Resources, Chinese Academy of Sciences, Lanzhou 730000, China

Abstract: For the safety of railroad operations, sand barriers are utilized to mitigate wind-sand disaster effects. These disasters, characterized by multi-directional wind patterns, result in diverse angles among the barriers. In this study, using numerical simulations, we examined the behavior of High Density Polyethylene (HDPE) sheet sand barriers under different wind angles, focusing on flow field distribution, windproof efficiency, and sedimentation erosion dynamics. This study discovered that at a steady wind speed, airflow velocity varies as the angle between the airflow and the HDPE barrier changes. Specifically, a 90° angle results in the widest low-speed airflow area on the barrier's downwind side. If the airflow is not perpendicular to the barrier, it prompts a lateral airflow movement which decreases as the angle expands. The windproof efficiency correlates directly with this angle but inversely with the wind's speed. Notably, with a wind angle of 90°, wind speed drops by 81%. The minimum wind speed is found at 5.1H (the sand barrier height) on the barrier's downwind side. As the angle grows, the barrier's windproof efficiency improves, extending its protective reach. Sedimentation is most prominent on the barrier's downwind side, as the wind angle shifts from 30° to 90°, the sand sedimentation area on the barrier's downwind side enlarges by 14.8H. As the angle grows, sedimentation intensifies, eventually overtakes the forward erosion and enlarges the sedimentation area.

Keywords: Multi-wind direction; HDPE sheet sand barrier; Numerical simulation; Windproof efficiency; Sedimentation erosion

1 Introduction

Wind-sand activities are natural geographic

events characterized by phenomena such as the forward progression of quicksand, land wind erosion, desertification, and the activation and movement of fixed dunes. These processes culminate in wind-driven sand erosion, transport, and accumulation. Western China has long grappled with these disasters, which have stymied its transportation development. Over recent decades, while China has built many desert railroads, they often suffer disruptions from such disasters. Hence, addressing the effects of wind-sand disasters is crucial to ensuring the sustainability and operation of railroads in Northwest China (Raffaele et al. 2019; Qu et al. 2007; Li et al. 2016). For decades, continuous innovations in sand prevention and control have led to notable contributions from scholars in mitigating wind-sand disasters (Chen et al. 2019; Parsons et al. 2004; Gillies et al. 2017; Cheng et al. 2016). Currently, three main strategies exist for wind-sand protection: mechanical (Bruno et al. 2018; Sun et al. 2004; Wang et al. 2017), chemical (Tie et al. 2013; Wang et al. 2005; Lai et al. 2017), and biological (Hesp et al. 2019; Xiao et al. 2004; Zhang et al. 2023). Biological strategies are often deemed the most effective. Yet, the challenging environment of Northwest China, with its barren terrains and limited rainfall, hampers the implementation of plant-based solutions. Chemical methods, meanwhile, have seen restricted use due to their economic and environmental implications. Consequently, mechanical methods have become the preferred approach in combating wind-sand disasters.

Alpine and arid terrain in northwest China necessitates the use of traditional wind and sand protection materials, such as wheatgrass and reeds. However, the limited lifespan of these materials, combined with increasing demand, has resulted in their scarcity. Consequently, there is an emerging shift towards alternative, more sustainable materials for wind and sand protection. A prominent alternative is HDPE (High Density Polyethylene). Renowned for its resistance to cold, heat, and ultraviolet rays, HDPE is also favored for its efficient construction process. It is particularly suitable for designing sand-blocking barriers in areas like northwestern China, which are prone to wind-sand calamities (Zhang et al. 2021). Research has increasingly focused on the effectiveness of HDPE sheet sand barriers. Zhang et al. (2019), through numerical simulations, highlighted that HDPE barriers with a 50% porosity offer optimal protection. They recommended installing three successive barriers spaced 30 m apart for best results. In a related study, Li et al. (2019) undertook on-site evaluations in the Gobi region of South Xinjiang, elucidating how HDPE barriers counter wind-sand and gauging their protective efficacy. Qu et al. (2014), using wind tunnel experiments, differentiated between various HDPE barrier designs, weighing the merits of both uniform and functional barriers. Complementing this, Qi et al. (2021) explored the HDPE barrier's ability to mitigate flow fields and its comprehensive role in wind-sand defense using similar testing techniques.

Research from around the globe highlights the protective merits of sand barriers (Wang et al. 2018; Rosenbrand et al. 2022; McClure et al. 2017). These studies emphasize the role of geometry, opening size, and notably, porosity, in determining a barrier's aerodynamic and morphodynamic properties. Indeed, porosity emerges as the pivotal factor for effective protection (Li et al. 2015; Li et al. 2023). For instance, wind tunnel experiments by Yu et al. (2012) revealed that barriers with porosities of 36% to 56% are most adept at combating wind-sand flow. Lima et al. (2020) further corroborated this through numerical simulations, noting that when porosity hits 40%, the barrier's vortex flow diminishes, bolstering its protective range. Similarly, Dong et al. (2006) identified a porosity range of 30%-60% as optimal for shielding. Drawing from these insights, barriers with porosities between 40% and 60% are deemed most effective. Consequently, our analysis focuses on a barrier with a 50% porosity.

Research into wind-sand disaster protection primarily centers on how variations in wind speed, airflow characteristics, and wind-sand blocking capabilities affect sand barriers' benefits, especially when the airflow is directly perpendicular to these barriers (Sun et al. 2017). Yet, there's an overlooked area regarding the efficacy of sand barriers under different wind angles. In practical settings, elements like topography and constructional design influence the wind-sand flow direction. Moreover, with railroads often having curved layouts, sand barriers, which are usually parallel to them, continuously face varying angles with the wind-sand flow. Notably, the Golmud–Korla Railway is heavily impacted by wind-sand disasters (Cui et al. 2018; Liang et al. 2018) and presents these challenges. Thus, a comprehensive study on the protection offered by sand barriers around the Golmud–Korla Railway across multiple

wind directions is crucial.

This research investigates the effects of varying wind directions on wind-sand flow, centering on the Golmud–Korla Railway. Through numerical simulations, this paper evaluates the efficacy and mechanisms of the HDPE sheet sand barrier at different wind angles.

2 Study Area

The study centers on the Gobi terrain near Mangya Lake within the Qinghai stretch of the Golmud–Korla Railway. This region is characterized by its dominant Gobi landform and a rich deposit of surface sand. Strong winds often stir these sand particles, forming wind-sand flows that jeopardize the railway's integrity. As depicted in Fig. 1(a), data from May 2019 to May 2020 provides insight into wind patterns. It indicates that the primary wind directions, namely WNW, NW, and W, account for 59.7% of the annual Sand-driving wind. Conversely, secondary wind directions, WSW and NNW, represent 17.1%. Fig. 1(b) uses Fryberger and Dean's (1979) formula to showcase the annual sand drift potential (DP), which stands at 223.56 VU, placing it in a medium wind energy category. Of this, WNW, NW, and W contribute to a potential of 196.24 VU, or 87.8% of the total. Further, the annual sand resultant drift potential (RDP) measures 186.93 VU, with the sand resultant drift direction (RDD) of 122.68°. The rate of change in sediment transport potential direction, RDP/DP, equals 0.836, signaling a single-peak wind condition.

3 Research Method and Validation

3.1 Computational model

3.1.1 Mathematical model

In this study, we utilize a three-dimensional steady-state Reynolds-averaged Navier-Stokes (RANS) model, based on the finite volume method, for our simulations. The timescale for sand transport significantly surpasses that for turbulence characteristics. This difference justifies neglecting non-constant flow, making the RANS method ideal for modeling wind-sand two-phase flow. We've incorporated the SST k-ω turbulence model, proven effective in numerical simulations of solid sand barriers and blunt body aerodynamics (Bruno et al. 2015).
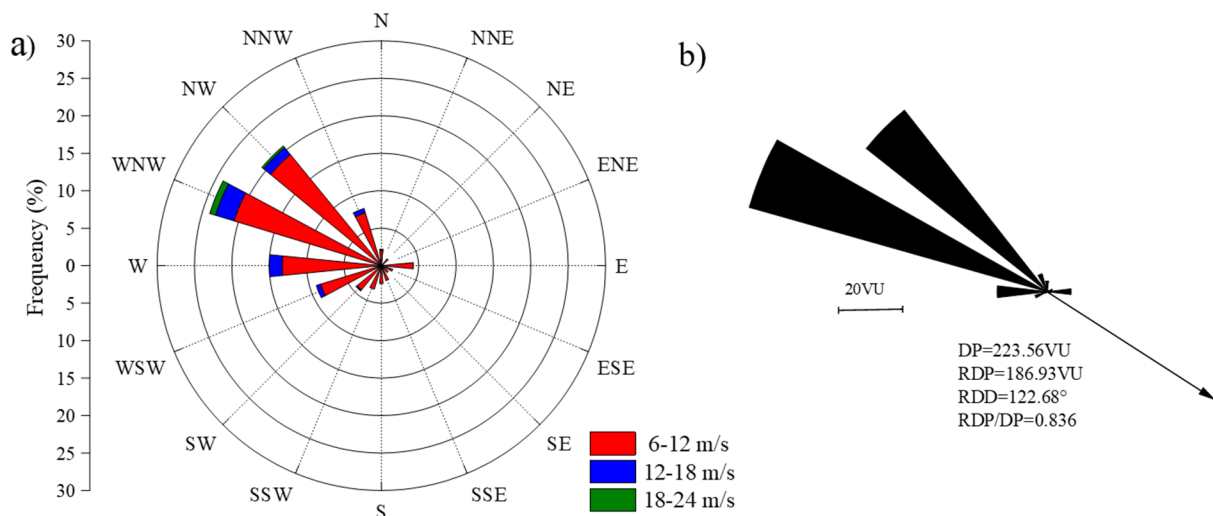
The control equation is presented as:

$$\frac{\partial \overline{V_i}}{\partial X_i} = 0 \tag{1}$$

$$\overline{V_j}\frac{\partial \overline{V_i}}{\partial X_i} = -\frac{1}{\rho}\frac{\partial \overline{P}}{\partial X_i} + \left[\mu\left(\frac{\partial \overline{V_i}}{\partial X_j} + \frac{\partial \overline{V_j}}{\partial X_i}\right)\right] - \frac{\partial}{\partial X_j}\left(\overline{V_i'V_j'}\right) \tag{2}$$

$$\overline{V_j}\frac{\partial k}{\partial X_i} = \frac{\partial}{\partial X_i}\left[\left(\sigma_k\mu_t + \mu\right)\frac{\partial k}{\partial X_i}\right] + \overline{P}_k - \beta^* k\omega \tag{3}$$

$$\overline{V_j}\frac{\partial \omega}{\partial X_i} = \frac{\partial}{\partial X_i}\left[\left(\sigma_\omega\mu_t + \mu\right)\frac{\partial \omega}{\partial X_i}\right] + C_{w1}\frac{\omega}{k}P_k$$
$$-C_{w2}\omega^2 + \left(1 - F_1\right)\frac{2\sigma_\omega}{\omega}\frac{\partial k}{\partial X_i}\frac{\partial \omega}{\partial X_i} \tag{4}$$

where $\overline{V_i}$ and $\overline{V_j}$ is the average velocity component, $\overline{V_i'}$ and $\overline{V_j'}$ is the pulse velocity component, X_i and X_j is the

Fig. 1 a) Rose diagram of wind speed and wind direction of sand-driving; b) Rose diagram of annual sand drift potential. DP means sand drift potential, RDP means sand resultant drift potential, RDD means sand resultant drift direction.

i and j direction along the x axis, μ is the kinematic viscosity of air, $\mu_t = k/\omega$ is the turbulent kinematic viscosity, $\overline{P}$ is the average pressure, ρ is the density of air, k is the turbulent kinetic energy, ω is the specific dissipation rate, P_k is the turbulent kinetic energy generation term due to the mean velocity gradient. The kinetic energy generation term $\tilde{P}_k$ is simulated by introducing a limiter to prevent turbulence in the stagnation region.

$$\tilde{P}_k = min(P_k, 10\beta^* k \omega), P_k \approx \mu_t \frac{\partial \overline{V}_i}{\partial X_j} + \frac{\partial \overline{V}_j}{\partial X_i} \frac{\partial \overline{V}_i}{\partial X_j} \quad (5)$$

The constants β^*, σ_k, σ_ω, C_{w1} and C_{w2}, as well as the hybrid function F1, follow the specifications set by Horvat et al. (2021). To precisely gauge the effect of aerodynamic roughness on the wind velocity profile, the SST k-ω model was enhanced with a sand roughness wall function tailored to the near-wall surface.

In our numerical simulation, factors like temperature and velocity primarily influence fluid compressibility. Given the assumptions of a 20°C temperature and a peak wind speed of 20 m/s, we obtain a Mach number under 0.3. Using these criteria and drawing on Nagata et al. (2016), we regard the fluid as incompressible. The movement of wind and sand exemplifies gas-solid two-phase flow. Adopting the Eulerian-Eulerian methodology, both phases – gas and sand – are treated as continuous media through the Eulerian approach. The pertinent equations are outlined below:

$$\text{gas phase: } \frac{\partial}{\partial t}(\varphi_g \rho_g v_g) + \nabla \cdot (\varphi_g \rho_g v_g v_g) \quad (6)$$
$$= -\varphi_g \nabla p + \nabla \cdot \tau_g + f_{sg} + \varphi_g \rho_g g$$

$$\text{solid phase: } \frac{\partial}{\partial t}(\varphi_s \rho_s v_s) + \nabla \cdot (\varphi_s \rho_s v_s v_s) \quad (7)$$
$$= -\varphi_s \nabla p - \nabla p_s + \nabla \cdot \tau_s + f_{sg} + \varphi_s \rho_s g$$

where φ_g and ρ_g is the gas phase volume fraction and density, φ_s and ρ_s is the solid phase volume fraction and density, and $\varphi_g + \varphi_s = 1$, p is the two-phase shared pressure, P_s is the solid phase pressure, g is the acceleration due to gravity, f_{sg} is the force between the two phases, v_g and v_s is the velocity of the gas and solid phases, τ_g and τ_s is the stress-strain tensor for gas and solid phases.

The three-dimensional model is illustrated in Fig. 2, with the coordinate origin positioned at the lower wall surface's entrance. Constructed from HDPE sheet, the sand barrier height (H) of 1.5 m, a thickness of 2 mm, and a porosity of 50%, indicating that half the barrier's area is void. These voids are sized at 12 cm × 4 cm each. The sand barrier interacts with the wind-sand flow at angles (α) of 30°, 45°, 60°, and 90°, which are close to the actual wind conditions. Determining the appropriate size for the computational domain is a pivotal aspect of the modeling process, as emphasized by Bradley et al. (1983). A domain that's too narrow an area may result in underdeveloped airflow, affecting the accuracy of results. On the other hand, an excessively large domain increases mesh numbers, leading to computational inefficiencies. After careful consideration, especially concerning boundary conditions, we set the computational domain dimensions to 100H × 10H × 20H. Through methodical trial calculations, we also defined a 40H distance between the center of the sand barriers and the watershed inlet.

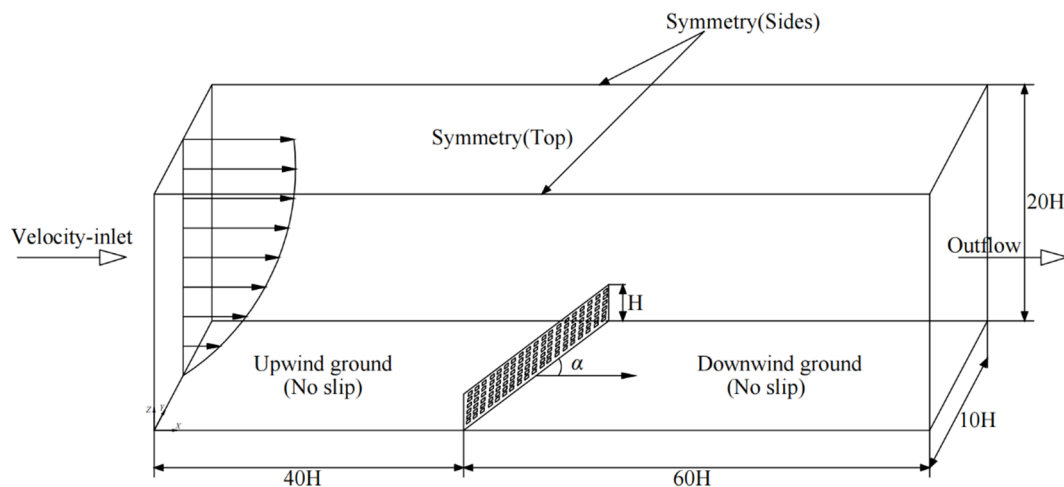Fig. 2 presents the boundary conditions for the

Fig. 2 Schematic of 3D model of HDPE sheet sand barrier.

computational domain. The domain's left side is a Velocity-inlet, and the right is an Outflow. The front, back, and top are labeled as Symmetry. The bottom wall and the sand barricade surface are both termed Wall, as elaborated in Table 1. Logarithmic winds define the inlet, leading to the subsequent velocity profile:

$$V_0(z) = \frac{u_0^*}{K} \ln \frac{z}{z_0} \qquad (8)$$

where $V_0(z)$ is the velocity at height z above the ground surface, u_0^* is the frictional wind speed, K is the von Kármán coefficient, taken as K = 0.4, z_0 is the aerodynamic roughness length, take z_0= 0.003 m (Zhang et al. 2021).

Table 1 Boundary condition setting the table

| Setting	Boundary condition
Velocity-inlet	$V_0(z) = \frac{u_0^*}{K} ln \frac{z}{z_0}$
Outflow	$\frac{\partial}{\partial X}(U, V, W, k, \varepsilon) = 0$
Symmetry	$V_{gx} = V_{gy} = 0$, $\frac{\partial \overrightarrow{V_g}}{\partial Y} = \frac{\partial \overrightarrow{V_s}}{\partial Y} = 0$
Wall	No slip, fixed boundary

3.1.2 Numerical method

For optimal mesh quality, we employed the Tetrahedrons method within Workbench Mesh for our model's unstructured meshing. This is evident in Fig. 3(a), which showcases the mesh across the entire computational domain. A close look at Fig. 3(b) reveals that we enhanced computational accuracy by meticulously refining the mesh near the sand barriers. It was essential to maintain the boundary layer height vertically to guarantee an adequate grid resolution, thereby effectively tackling the flow variable gradient

issue (Blocken et al. 2007). The grid adheres to the wall surface's functional criteria, represented as $30 < n^+ = n_p u_0^*/\mu < 200$, where n_w denotes the height of the boundary layer grid, and n_p is the midpoint height of that layer. The bottom wall was structured with 10 boundary layers, expanding at a rate of 1.2. Grid quantities differ depending on the sand barriers used and the size of the computational domain. For instance, a 90° wind angle model encompasses roughly 2.8×10⁶ grids, whereas a 30° model houses about 4.5×10⁶ grids. All other models fall within this grid count range and maintain a tilt rate below 0.7, indicative of the grid's superior quality, meeting the numerical simulation criteria.

Our model uses a three-dimensional pressure solver for accuracy. To further improve precision, a double-precision calculation method is employed. Given the trade-off between hardware capabilities and desired accuracy, we chose the Simple algorithm, which is renowned for its precision (Wang et al. 2018). For areas near the wall, Standard Wall Functions are utilized to ensure accurate results. When computing solutions, the second-order windward format is chosen for the discrete convection term, while the center-difference format is used for the discrete diffusion term. Iterations proceed in 0.1s intervals, targeting a convergence residual of 10⁻⁵.

3.1.3 Incoming winds and sand characteristics

For this simulation, we calibrated our parameters based on the Golmud−Korla Railway's observed incoming wind speeds. At 10 m from the sand inflow inlet's surface, we established incoming wind speeds of 8, 12, 16, and 20 m/s. These speeds correspond to drag wind speeds u_0^* at the inlet of 0.46, 0.56, 0.65, and 0.75 m/s, respectively. Importantly, these values exceed the critical drag wind speeds u_0^* required to cause erosion for the range of sand particle diameters $d \in [0.063, 1.2]$
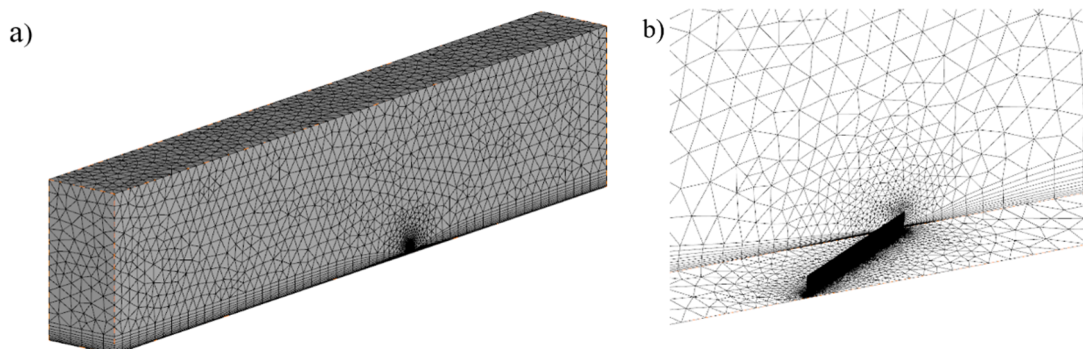
Fig. 3 (a) Overall computational domain grid; (b) Localized regional grid around sand barriers.

mm (Kok et al. 2012).

In our wind-sand flow simulation, the parameters are set as follows: a sand particle size d=0.1 mm; sand density ρ_s=2650 kg/m³; sand phase volume fraction of 0.01; air density ρ_a =1.225 kg/m³; and aerodynamic viscosity μ=1.7894×10⁻⁵ Pa·s.

3.1.4 Data processing

Windproof efficiency, as outlined by Zhang et al. (2022), measures how much wind speed decreases after flows through a sand barrier. Evaluating this efficiency reveals changes in wind speed around these sand barriers. The calculation for this efficiency is based on the formula:

$$\varphi_{XZ} = \left(1 - \frac{V_{XZ}}{V'_{XZ}}\right) \times 100\% \qquad (9)$$

where φ_{XZ} is the windproof efficiency of the HDPE sheet sand barrier, V_{XZ} is the wind speed at the downwind ground (X, Z) point after the airflow passes through the sand barrier, V'_{XZ} is the horizontal wind speed when the airflow is not disturbed.

3.2 Validation

3.2.1 Wind tunnel test design

A wind tunnel test took place at the Gansu Institute of Desertification Research, specifically in the key laboratory specializing in desertification and wind-sand disaster mitigation. The wind tunnel, measuring 16 m in length, boasts a cross-sectional area of 1.2 m×1.2 m and a boundary layer 0.5 m thick. During the experiment, wind speeds were adjusted to 8, 12, 16, and 20 m/s, with angles of 45° and 90° tested between the airflow and sand barrier placement. The sand barrier model, featuring a 50% porosity, had dimensions of 1.1 m×0.002 m×0.15 m. A visual layout can be seen in Fig. 4. The scale between the wind tunnel and the numerical simulation was set at 1:10. Given the wind tunnel's blockage ratio stood at 5.7%, it satisfied geometric similarity standards (Wu et al. 2013).

To ensure that both the numerical simulation and the wind tunnel test are based on the same initial boundary conditions, this study compared their wind speed profiles at the entrance, as illustrated in Fig. 5. The data from both sources aligns well, following the logarithmic motion law without significant variations in the wind speed gradient patterns, thus satisfying the motion similarity (Zhang et al. 2023). In the wind tunnel test, we selected four inlet wind speeds. The Reynolds number, represented by Re = $\rho v L/\mu$ (with Re for the flow Reynolds number, ρ for air density, v for the flow's characteristic velocity, L as the characteristic length, and μ as the kinematic viscosity), spans from 8.26×10⁵ to 2.06×10⁶. Importantly, once the Reynolds number surpasses 10⁵, the behavior of the fluid becomes stable despite any additional increase in the Reynolds number, denoting the attainment of kinetic similarity (White 1996; Zhang et al. 2020). Consequently, this wind tunnel test meets the standards of geometrical, kinematic, and dynamic similarity in line with the established similarity principle (Raffaele et al. 2021).

3.2.2 Validation of results

During the experiment, this study used a Bitot tube to measure the wind speed around the sand barriers, collecting data at a 2 Hz frequency over a span of 60 s. We focused on contrasting the results of the wind tunnel test and the numerical simulation,
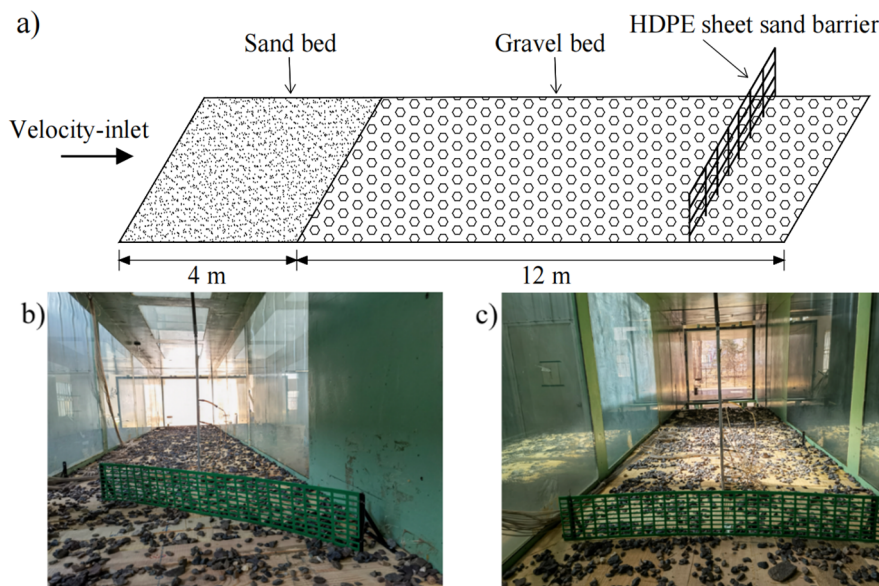

Fig. 4 Wind tunnel test layout: a) sketch of wind tunnel test layout; b) layout when the angle between the airflow and the sand barrier is 45°; c) layout when the angle between the airflow and the sand barrier is 90°.

particularly for conditions with a wind speed of 12 m/s and an angle of 45°. The outcomes of this comparison are depicted in Fig. 6. The figure illustrates that the horizontal wind speeds from both methods display a consistent trend. There are slight discrepancies between certain wind tunnel results and numerical simulations, yet on the whole, the datasets are remarkably aligned. This alignment attests to the accuracy of the numerical simulation in replicating real-world airflow conditions, validating the flow field settings used in the simulation.
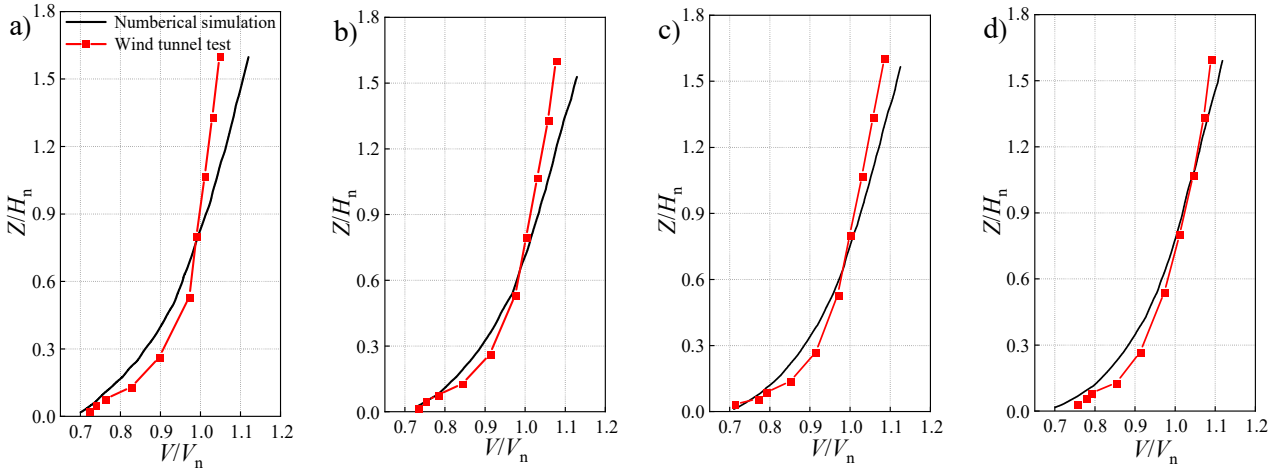
Fig. 5 Comparison of wind tunnel test data and numerically simulated wind speed contours at the entrance (H_n represents the sand barrier heights H and H1 in the numerical simulation and wind tunnel test, respectively, and V_n represents the velocity V and $V1$ at the height of the sand barrier in the numerical simulation and wind tunnel test, respectively.): a) 8 m/s; b) 12 m/s; c) 16 m/s; d) 20 m/s.
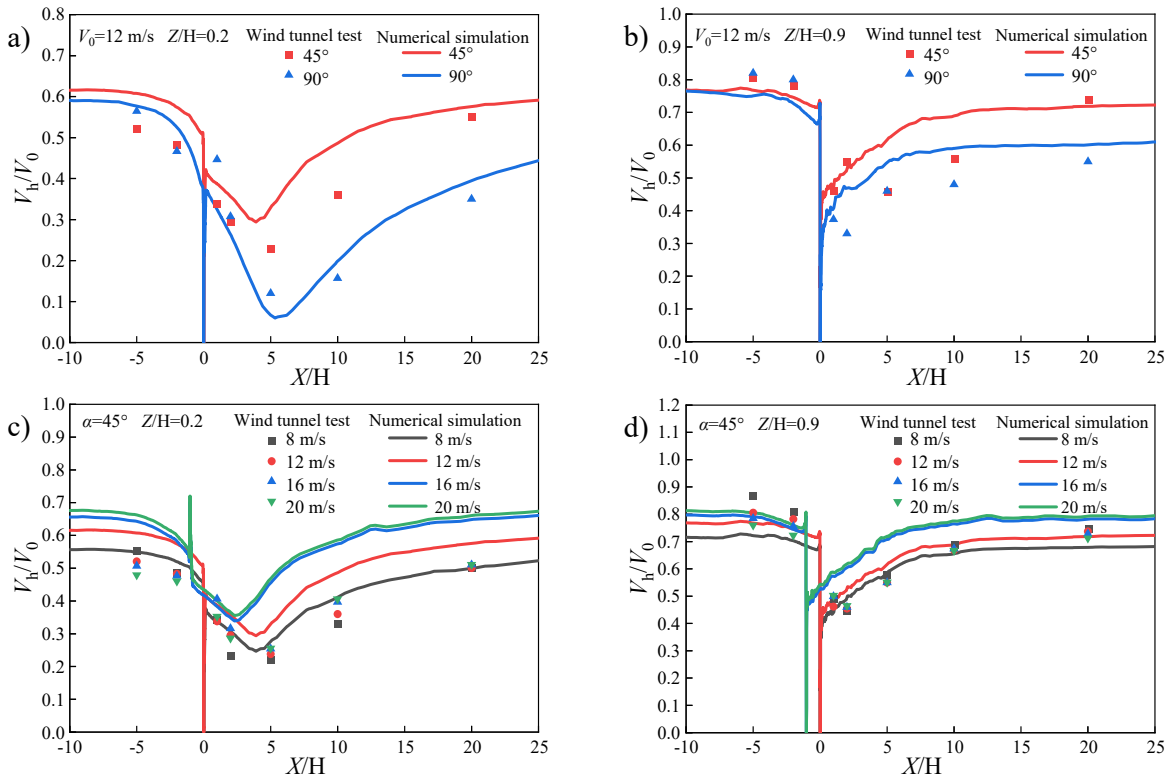
Fig. 6 Comparison of the results of wind tunnel test and numerical simulation: a) V_0=12 m/s, Z/H=0.2; b) V_0=12 m/s, Z/H=0.9; c) α=45°, Z/H=0.2; d) α=45°, Z/H=0.9 (V_0 is the incoming wind speed at the Velocity-inlet, V_h is the velocity at height h above the ground surface.)

4 Simulation Results and Discussion

4.1 Structural characteristics of the flow field

### 4.1.1 Variations in flow field with incoming wind speeds

In order to understand the airflow patterns around the sand barrier, we examined the flow field at the Y = 7.5 m section of the computational profile. This examination provides insights into the airflow changes with different wind speeds and directions.

Fig. 7 depicts the velocity flow field around sand barriers when subjected to different wind speeds at a 30° angle with the airflow. This illustration demonstrates a remarkable consistency in the flow field's characteristics regardless of the wind speed. Yet, variations are evident in the defined partitions. As the wind-sand flow approaches the barriers, it encounters resistance, creating a low-speed zone—Area A—on the windward side. Upon contact with the barriers, a segment of the airflow rises due to this obstruction, generating a high-speed zone, Area B, over the barriers. In contrast, the residual flow navigates through the barrier pores, establishing a low-speed zone, Area C, on the leeward side. Continuing on the leeward side, the airflow's speed gradually recovers, transitioning into Area D: the dissipation recovery zone. The airflow pattern around the sand barriers mirrors findings by Chen et al. (2019) and Ding et al. (2021). Past this D zone, the airflow proceeds unhindered, reverting to its uninfluenced state. Evaluating the airflow distribution on the leeward side across varying wind speeds, it becomes apparent that an uptick in speed shifts the stabilization point—marked by a red dot—further from the barriers. This trend underscores that greater wind speeds yield broader partitioned regions.

4.1.2 Variations in flow field with wind angles

At an incoming wind speed of 12 m/s, variations in the velocity flow field around the sand barriers emerge based on different wind angles, as depicted in Fig. 8. As the angle between the airflow and the sand barrier widens, there's a marked reduction in airflow velocity within the same area. Particularly at 60° and 90° angles, the velocity in Zone C, the low-speed section on the leeward side of the barrier, decreases considerably. This decrease is a result of the notable difference in velocity between the high-speed Zone B and low-speed Zone C, both located on the barrier's leeward side. This difference creates a reverse pressure gradient, culminating in the establishment of a low-speed recirculation zone, highlighted by the negatively-valued red region. At a direct 90° angle to the barriers, this zone becomes broader and slower. Zhang et al. (2023) conducted research on the flow field around embankments under different wind angles. They found that at this 90° angle, the low-speed region on the leeward side becomes more expansive, a result consistent with our observations. In summation, as the angle between the airflow and the barriers increases, the partitioning characteristics of the airflow grow more pronounced, amplifying the dynamics
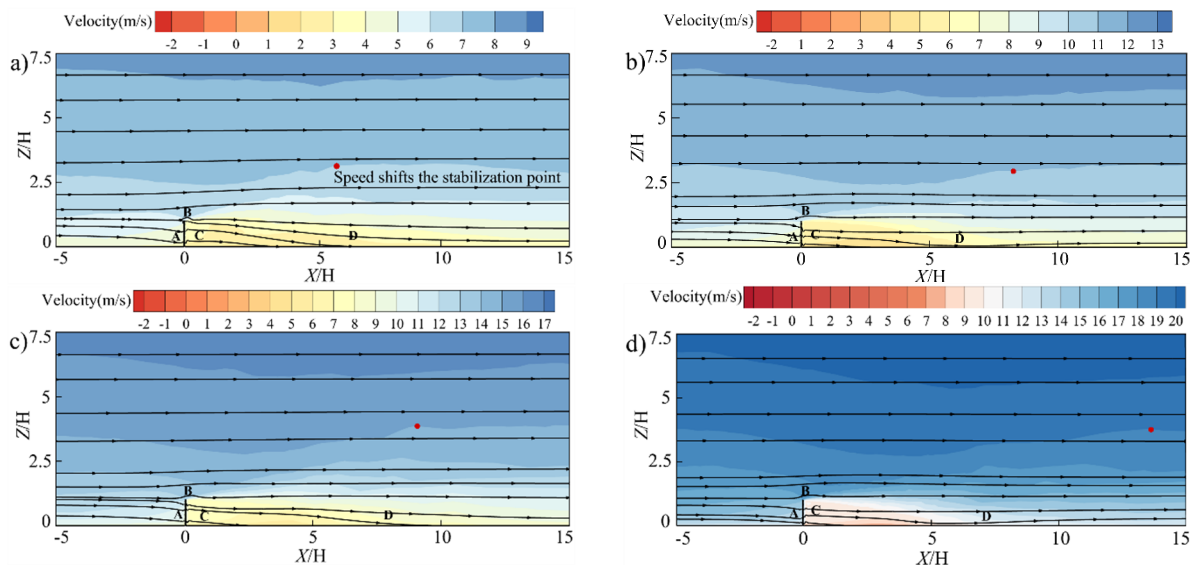
Fig. 7 Velocity flow field cloud diagram around the HDPE sheet sand barrier at different incoming wind speeds when the angle between the airflow and the sand barrier is 30°: a) 8 m/s; b) 12 m/s; c) 16 m/s; d) 20 m/s (A is the windward side low-speed zone, B is the high-speed zone, C is the leeward side low-speed zone, and D is the dissipation recovery zone.)
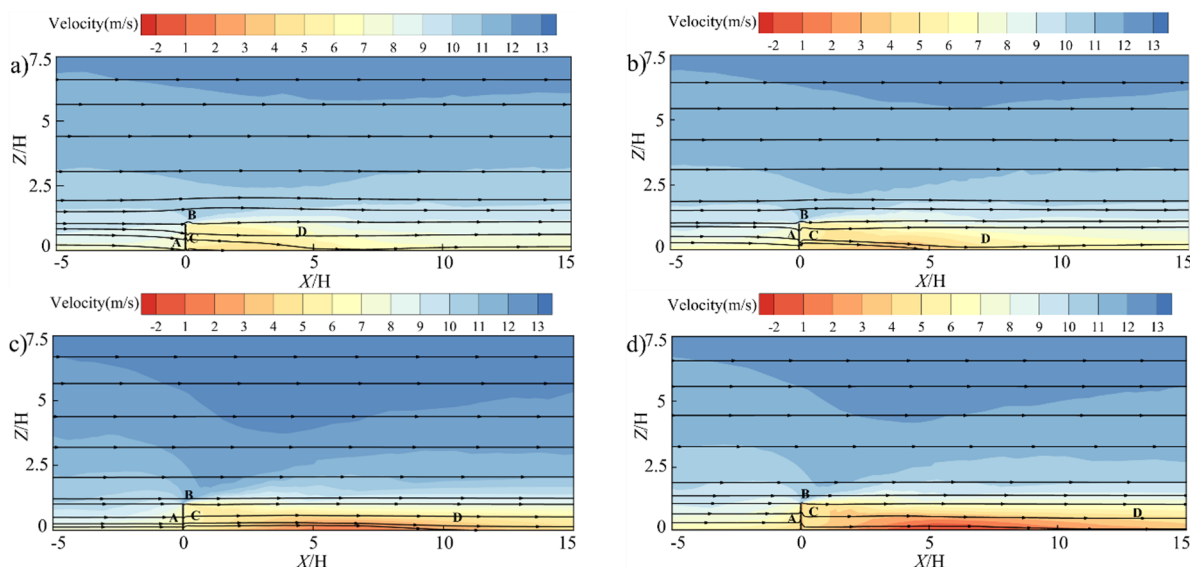
Fig. 8 Velocity flow field cloud diagrams around the HDPE sheet sand barrier at different wind angles when the incoming wind speed is 12 m/s: a) 30°; b) 45°; c) 60°; d) 90°.

between the high and low-speed zones on the barrier's leeward side. In a related study, Sun et al. (2023) assessed the wind protection of mechanical sand barriers fitted with porous sand-fixing bricks, using wind tunnel tests. They highlighted the wind pressure sensitivity on sand barriers due to changes in wind angle. The most significant drop in wind speed on the barriers' leeward side occurred when the wind directly faced the barriers. This observation aligns with our findings, underscoring the optimal protective capacity of the sand barriers at a 90° wind direction.

4.1.3 Airflow trajectories with different wind angles

Using the three-dimensional trajectory map in Fig. 9, we provide a detailed representation of the airflow patterns around sand barriers at different wind angles. The map distinctly shows the variations in airflow trajectories at a height range of H above the ground. At a 30° angle between the airflow and the barriers, there's a noticeable lateral trajectory on the leeward side. When the angle between the airflow and the sand barrier is 90°, the lateral motion trajectory of the airflow completely disappears. Horvat et al. (2021) found that larger wind angles yield broader sand sedimentation areas near tracks. This corroborates our observation that the most significant airflow attenuation around the sand barrier arises at a direct 90° wind angle. This attenuation results from the reduced lateral motion of the airflow at this 90° wind angle, which in turn lessens its interaction with the barriers' opposing movement.
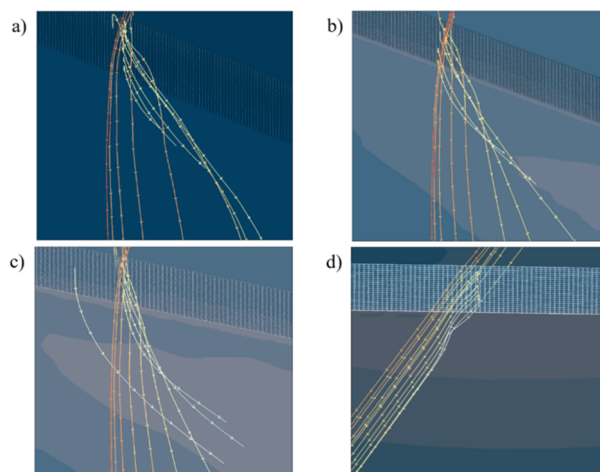
Fig. 9 Trace plot of airflow trajectories around the HDPE sheet sand barrier at different wind angles: a) 30°; b) 45°; c) 60°; d) 90°.

4.2 Characteristics of wind speed variations

4.2.1 Effects of incoming wind speeds on horizontal wind speed

In this study, the variations in horizontal wind speed around sand barriers at heights of z=0.1, 0.3, 0.5, 0.8, 1.5, and 2.0 m above the ground is examined. Fig. 10 presents the changes in horizontal wind speed around the sand barriers at different elevations when the angle between the airflow and the barriers is 30°. These patterns of horizontal wind speed consistently manifest across varying incoming wind speeds. At lower heights (z = 0.1, 0.3, 0.5, 0.8 m), the wind speed on the downwind side displays a "v" shaped pattern.

This "v" shape becomes more pronounced closer to the ground, indicating a significant decline in wind speed once the airflow bypasses the sand barrier, with an even sharper decrease near the surface. These observations align with those of Zhang et al. (2020). Interestingly, the wind speed trends at heights of 1.5 and 2 m deviate from the aforementioned patterns. Before the sand barrier, there's a modest dip in speed, but there's a noticeable surge in speed just above the barrier. This increase is attributed to part of the airflow being directed upwards over the barrier, leading to an acceleration. This phenomenon is in line with the findings described in Section 4.1. Overall, starting from the 10H point downwind, the horizontal wind speed approaches stability. Simultaneously, the V_h/V_o value

for each graph at this location gradually increases.

4.2.2 Effects of wind angles on horizontal wind speed

Fig. 11 illustrates the horizontal wind speed distribution around sand barriers at various wind angles, given an incoming speed of 12 m/s. Examining this figure, one observes a uniform pattern of wind speed changes at the barrier's lower elevations, specifically at $z=0.1$, 0.3, 0.5, and 0.8 m. To illustrate this point, $z=0.5$ m is chosen for detailed analysis. As wind angles change, significant variations appear in the speed distribution. There's an evident escalation in wind speed attenuation with the increase in angle magnitude. To put this into perspective, wind speeds
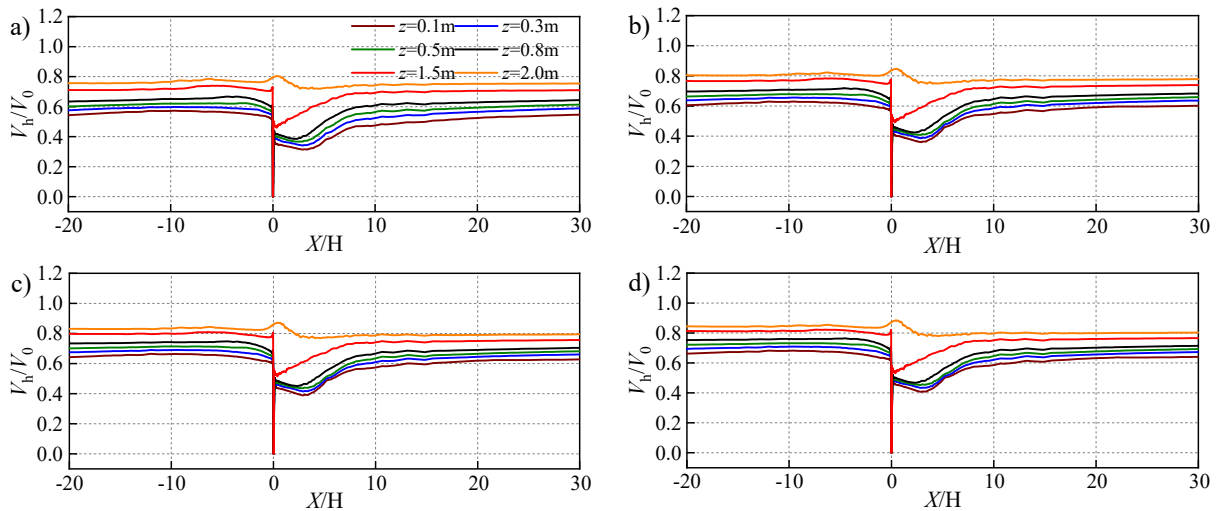
Fig. 10 Horizontal wind speed distribution patterns around the sand barriers at different wind speeds when the angle between the airflow and the sand barriers is 30°: a) 8 m/s; b) 12 m/s; c) 16 m/s; d) 20 m/s. (On the graph, the windward side of the sand barriers is located to the left of horizontal coordinate 0, while the downwind side is to the right).
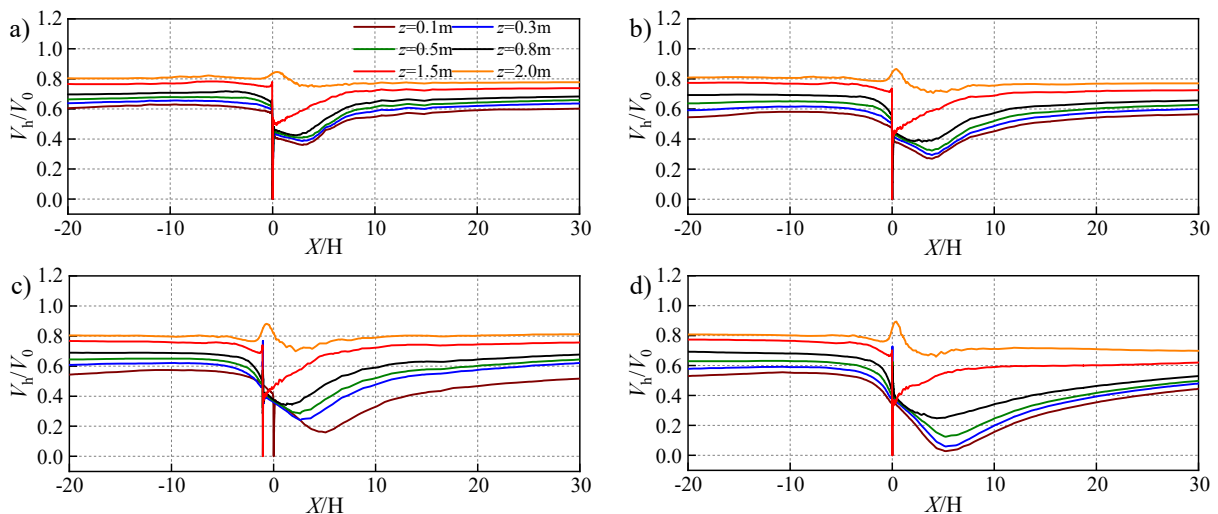
Fig. 11 Horizontal wind speed distribution patterns around the sand barriers at different wind angles when the incoming wind speed is 12 m/s: a) 30°; b) 45°; c) 60°; d) 90°.

decrease by roughly 40%, 48%, 62%, and 81% at angles of 30°, 45°, 60°, and 90°, respectively. This data suggests that the wind speed reduction at 90° is almost twice as profound as at 30°. Moreover, Fig. 11 highlights that as the angle becomes more acute, there's a broadening in the region where wind speed diminishes. At the aforementioned angles, the most significant reductions are recorded at distances of 2.7H, 3.6H, 4.4H, and 5.1H downwind from the barriers, respectively.

4.2.3 Wind speed profile changes with incoming wind speeds

Wind speed profiles illustrate the variation in speed with respect to height, as highlighted by Bauer et al. (2004). In order to elucidate the wind speed profiles at various locations within the basin, this study examines points both upwind and downwind of the sand barriers. We have chosen locations 5H (P1) and 2H (P2) upwind, as well as 1H (P3), 2H (P4), 5H (P5),

8H (P6), 10H (P7), and 15H (P8) downwind for detailed scrutiny. In our evaluation, we treat both Z and V_i as dimensionless. The horizontal coordinate is the ratio of velocity V_i to V_H for each site, whereas the vertical coordinate stems from the ratio of coordinate Z to the height H of the sand barrier. It should be noted that V_i encompasses velocities V_X in the X axis and V_Z in the Z axis. Meanwhile, V_H signifies the velocity observed at height H from the ground level.

Fig. 12 displays the wind speed profile around the sand barrier when the angle between the airflow and the barrier is set at 30°. It differentiates wind speeds in both X and Z directions: V_{X1} to V_{X4} and V_{Z1} to V_{Z4}, corresponding to incoming wind speeds of 8, 12, 16, and 20 m/s. This figure reveals a regular alteration in the wind speed profile near the sand barriers. Observations from positions P1 and P2 show contrasting behaviors. At P1, the V_Z/V_H ratio stays consistent vertically. However, at P2, this ratio becomes positive near a height of 1H, maintaining a
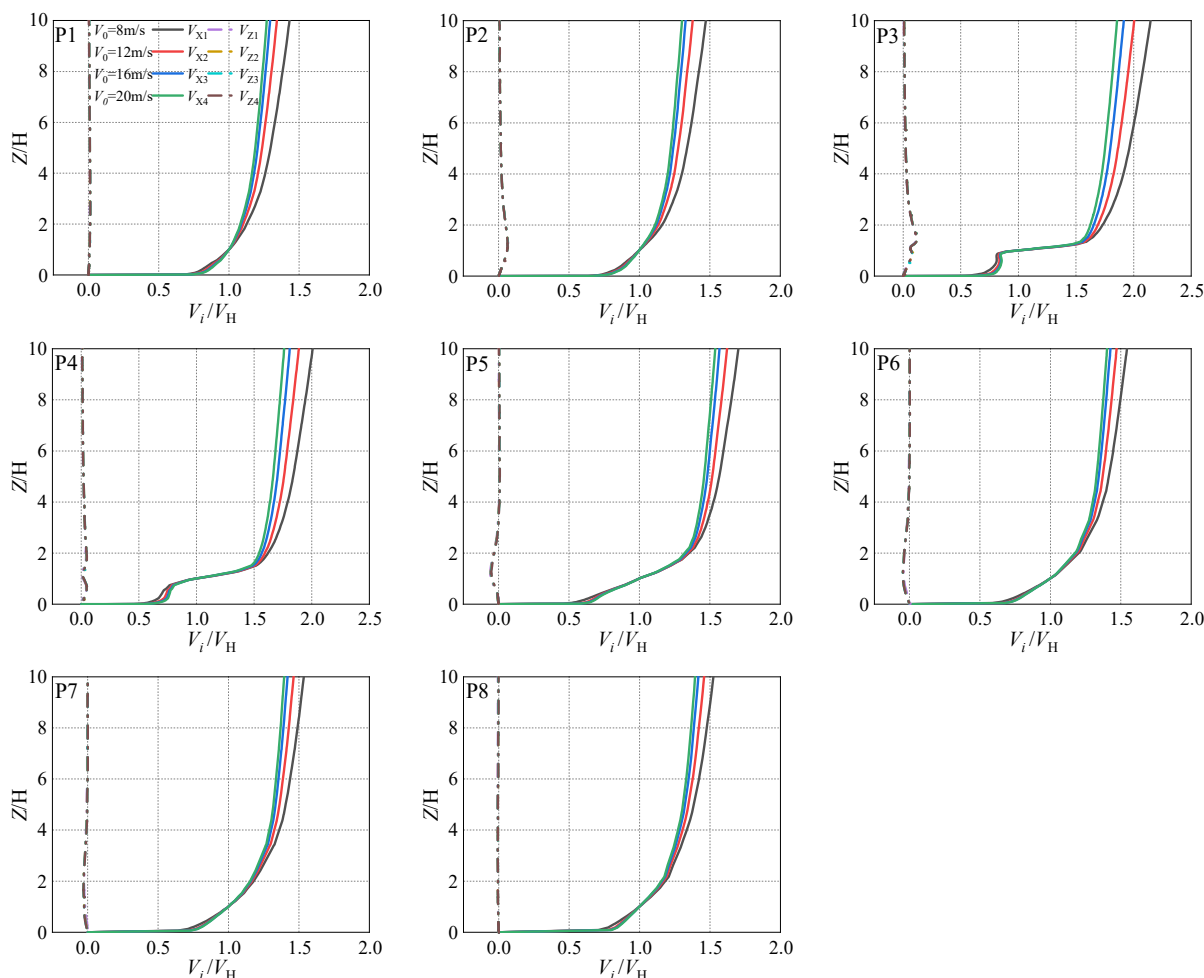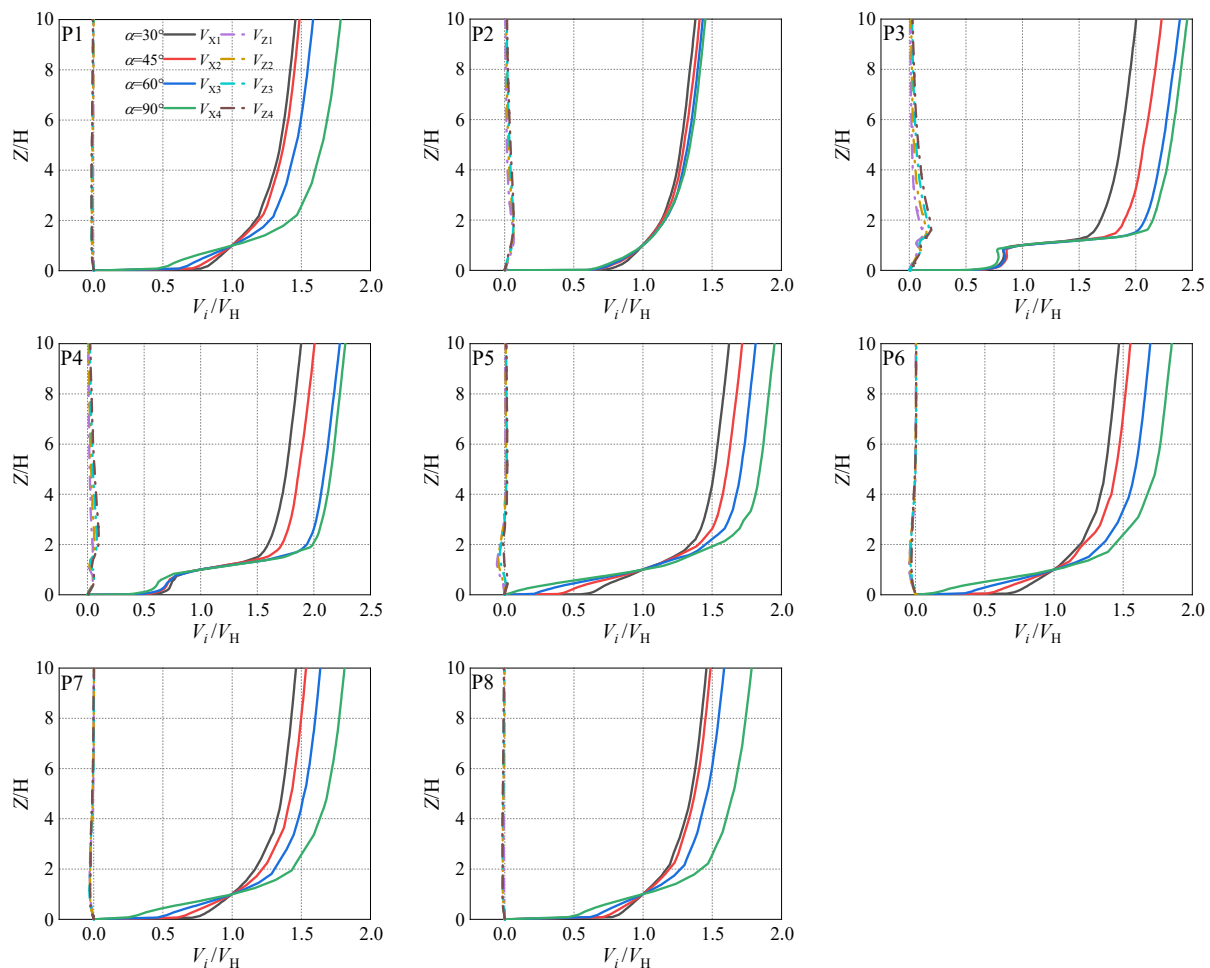

Fig. 12 Wind speed profiles around the sand barriers (P1-P8) at different incoming wind speeds when the angle between the airflow and the sand barriers is 30°.

steady rate of change across varying wind speeds. For the P3 and P4 points, the V_X/V_H showcases a segmented logarithmic growth, reaching up to the height H. Beneath this level, V_X/V_H increases with wind speed; above, it decreases. At further distances from the sand barriers, specifically between P5 and P8, there's a noticeable uptick in the slope of the V_X/V_H curve under the 2H mark, indicating a return to the logarithmic pattern for V_X/V_H. Guo et al. (2017) investigated wind speed profiles near sand barriers of different shapes and materials. Their research underscores that changes in the wind speed profiles around these barriers chiefly depend on the barriers' plane specification and exposed height. Thus, with rising incoming wind speed, the wind speed profiles variation pattern near the barriers stays consistent.

4.2.4 Wind speed profile changes with wind angles

Upon analyzing the wind speed profiles around the

sand barriers at varying incoming speeds, a consistent trend is observed. Using the wind speed of 12 m/s as an example (Fig. 13), the profiles labeled V_{X1} to V_{X4} and V_{Z1} to V_{Z4} denote wind speeds in the X and Z directions at airflow angles of 30°, 45°, 60°, and 90° to the sand barriers. In Fig. 13, the V_X/V_H ratio showcases a logarithmic trend at both the P1 and P2 positions. Interestingly, while the V_X/V_H remains consistent for 30° and 45° angles at the P2 position compared to P1, it reduces at 60° and 90°. This decrease highlights the enhanced efficacy of the sand barriers in wind resistance and sand blockage at steeper angles. At the P2 position, the barrier restricts airflow, constricting the flow area. As a result, some airflow is channeled above the barrier, requiring an increased flow rate for consistent volume. This shift creates an accelerated airflow zone on the barrier's upwind side, thus amplifying the V_Z/V_H values for different wind angles. Positions P3 and P4, situated close to and on the downwind side of the barrier, exhibit a segmented
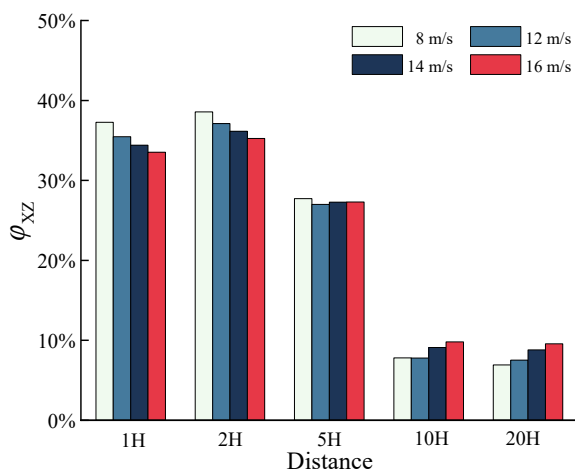

Fig. 13 Wind speed profiles around the sand barriers (P1-P8) at different wind angles when the incoming wind speed is 12 m/s.

logarithmic growth in V_X/V_H, distinguished by the height, H. The growth pattern below H originates from airflow through the barrier's pores, whereas above H, it arises from the overhead airflow. Starting from the P5 position, the V_X/V_H pattern deviates from this segmented trend and reverts to a standard logarithmic one, signaling a reducing impact of the barriers. This trend persists from positions P6 to P8, with a consistent decline in V_X/V_H as proximity to the barriers increases. Essentially, wind speed profiles in the X direction on the downwind side of the sand barriers exhibit a segmented logarithmic growth trend around height H, regardless of wind angles. Moreover, V_X/V_H values exhibit a negative correlation with wind angle below this height. In a related study, Yan et al. (2019) investigated wind speed profiles on open-air roadways under varying wind angles. Their findings underscored the significant influence of wind direction angle on wind speed profiles. As this angle widens, airflow velocity on the roadway's downwind side decreases more rapidly, aligning with our observations.

4.3 Windproof efficiency

In order to explore the influence of sand barriers on airflow, we evaluated the windproof efficiency downstream of the barriers at specific distances: 1H, 2H, 5H, 10H, and 20H. At each distance, we considered six distinct heights from the ground—0.1, 0.2, 0.3, 0.5, 0.8, and 1.5 m—to determine the efficiency. Subsequently, the average efficiency from these heights established the windproof efficiency for the respective distance.

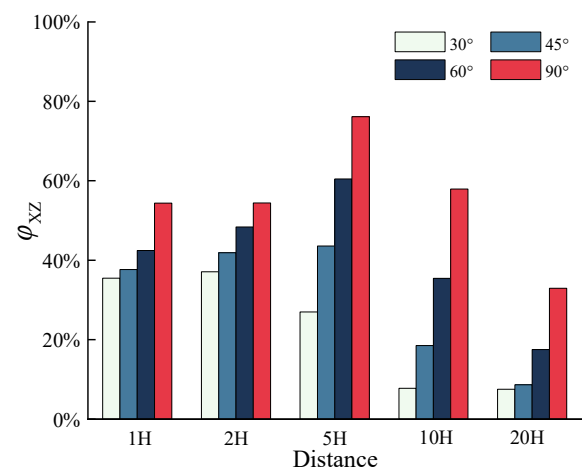Fig. 14 depicts the windproof efficiency of the sand barrier under different wind speeds with an airflow angle of 30°. The data reveals that at wind speeds of 8, 12, 16, and 20 m/s, the sand barriers exhibit peak efficiencies of 38.6%, 37.1%, 36.2%, and 35.3%, respectively. Interestingly, the highest efficiency consistently appears at the 2H position downwind from the barriers. The data also indicates a trend: with increasing wind speed, the barrier's windproof efficiency marginally decreases. Additionally, efficiencies at positions 1H, 2H, and 5H are considerably higher than those at 10H and 20H. Therefore, with a 30° airflow angle relative to the sand barrier, its primary protective range lies between 0 and 5H.

Fig. 15 depicts the windproof efficiency of sand barriers at various wind angles with a consistent incoming wind speed of 12 m/s. Specifically, at an airflow angle of 30° to the sand barrier, the highest efficiency peaks at 37.1% at the 2H downwind position. In contrast, at angles of 45°, 60°, and 90°, the top efficiencies are 43.6%, 60.5%, and 76.2%, respectively, all found at the 5H downwind position. This trend indicates that a larger airflow angle correlates with increased windproof efficiency. Furthermore, the data illustrates a notable efficiency trajectory on the downwind side of the barriers: it increases initially with distance, then tapers off.

4.4 Sedimentation-erosion characteristics

4.4.1 Sedimentation-erosion patterns with incoming wind speeds

The sedimentation and erosion patterns of sand near barriers depend largely on the local shear stress

Fig. 14 Windproof efficiency (φ_{xz}) around sand barriers at different incoming wind speeds when the angle between the airflow and the sand barriers is 30°.


Fig. 15 Windproof efficiency (φ_{xz}) around sand barriers at different wind angles when the incoming wind speed is 12 m/s.

on the surface and the sand's critical shear stress. This study introduces dimensionless ratios τ^* and $\tau^* = \frac{\tau_x}{|\tau_x|} \frac{|\tau|}{\tau_t}$ as outlined by Horvat et al. (2022). Specifically, τ pertains to the local shear stress on the surface, and τ_x to that in the X-direction. The sand particles' critical shear stress is represented by τ_t. In our simulations, with a sand particle diameter of d=0.1 mm, τ_t is equated to 0.045 Pa (Raffaele et al. 2016). Within this framework, $\tau^* = \pm 1$ sets the erosion threshold. Defined conditions include: $\tau^* > 1$ signaling the forward erosion zone; $-1 < \tau^* < 1$ designating the sedimentation zone; and $\tau^* < -1$ indicating the backward erosion zone as detailed by Bruno et al. (2018). The precise location where sedimentation and erosion intersect is labeled the sedimentation point.

Fig. 16(a) depicts how varying wind speeds impact the sand sedimentation and erosion around a sand barrier, especially when the airflow's angle with the barrier is 30°. The labels 1# to 4# in this figure correspond to the characteristic curves for wind speeds of 8, 12, 16, and 20 m/s, respectively. A consistent pattern emerges across these curves; for instance, the 1# and 2# curves follow a sequence: forward erosion, sedimentation, then forward erosion again. However, the 3# and 4# curves show only forward erosion. Fig. 16(b) delves into the specifics of sedimentation and erosion distances of sand particles near the barriers at these wind speeds, again at a 30° angle. At a wind speed of 8 m/s, the sand starts eroding on the upwind side of the barriers and begins sedimenting at 0.14H on the downwind side, lasting until 28.15H. Forward erosion then reoccurs from 28.29H. At 12 m/s, erosion occurs on the upwind side, with sedimentation beginning at 2.28H and continuing until 1.5H. Erosion then resumes from 3.78H. For the higher speeds of 16 and 20 m/s, the surrounding area primarily witnesses forward erosion. Conclusively, the data points to an inverse relationship between wind speed and sedimentation regions, with erosion areas expanding as wind speeds increase.

4.4.2 Sedimentation-erosion patterns with wind angles

Fig. 17(a) presents how sand sedimentation and erosion vary around sand barriers at different wind angles, given a constant incoming wind speed of 12 m/s. In this figure, labels 5# - 8# represent the characteristic curves for airflow-barrier angles of 30°, 45°, 60°, and 90°. Analysis of these curves underscores a consistent trend in sand sedimentation and erosion
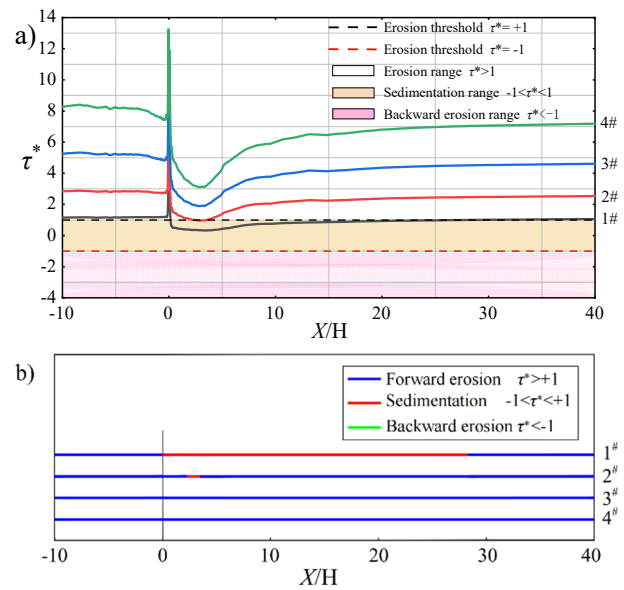
Fig. 16 Sedimentation and erosion around the sand barrier at different incoming wind speeds when the angle between the airflow and the sand barrier is 30°: a) τ^*; b) sedimentation and erosion distance of sand particles.
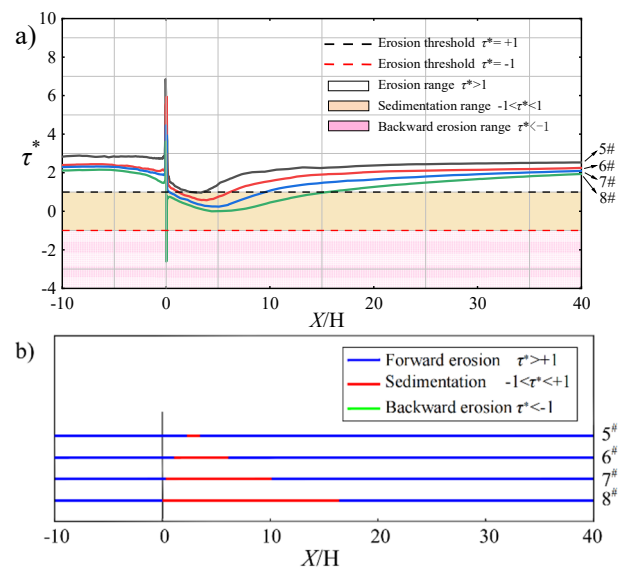
Fig. 17 Sand sedimentation and erosion around the sand barriers at different wind angles when the incoming wind speed is 12 m/s: a) τ^*; b) sedimentation and erosion distance of sand particles.

across these angles. Curves 5# - 7# can be categorized into three main regions: forward erosion, followed by sedimentation, and then forward erosion again. On the upwind side, forward erosion is dominant. Conversely, on the downwind side, as the angle between the airflow and barriers grows, the distance between two sedimentation points expands: the first point is nearer to the barriers, while the second is farther. The 8#

curve, however, comprises four distinct phases: forward erosion, backward erosion, sedimentation, and another forward erosion. It indicates forward erosion on the upwind side and backward erosion right at the barrier. As the angle reaches 90°, the gap between the barriers and the second sedimentation point reaches its maximum, highlighting the most extensive sedimentation area on the downwind side. As the angle between the airflow and the sand barrier widens, sedimentation on the downwind side increasingly supersedes the forward erosion. In essence, a broader angle leads to an expanded sedimentation zone on the barrier's leeward side. The research identifies two primary reasons behind this trend. Firstly, a sharp angle between the airflow and the barriers reduces their ability to shield against wind and capture sand. Secondly, the research utilized HDPE sheet barriers with a porosity of 50%. These aspects lead to a reduced vortex in the leeward airflow cyclone region. Furthermore, the airflow's reverse shear stress doesn't meet the critical threshold of sand particles, inhibiting any backward erosion. Fig. 17(b) illustrates the sedimentation and erosion distances of sand particles around sand barriers for different wind angles, given an incoming wind speed of 12 m/s. The labels 5# - 8# in the figure indicate sedimentation and erosion lengths for airflow-barrier angles of 30°, 45°, 60°, and 90°, respectively. At a 30° angle, the upwind region experiences forward erosion. Sedimentation begins at 2.28H on the downwind side, covering a distance of 1.5H, before forward erosion resumes at 3.78H. For a 45° angle, the upwind area is dominated by forward erosion. Sedimentation starts at 1.11H, spanning 5H, with forward erosion recommencing from 6.11H. At 60°, forward erosion is evident upwind, while sedimentation starts at 0.29H and stretches to 9.86H, with forward erosion returning at 10.15H. At 90°, despite the initial forward erosion upwind, sedimentation initiates at 0.11H, extends to 16.33H, and then forward erosion takes over from 16.44H. Conclusively, as the angle between the airflow and barrier increases, the sedimentation distance expands, starting nearer to the barrier and ending further away. In their study, Horvat et al. (2021) examined sedimentation and erosion characteristics near tracks under varying wind angles. Their findings suggest that, for the same incoming wind speed, smaller wind angles result in a larger erosion area near the track. Put simply, as the wind angle increases, the sedimentation area around the sand barriers also increases.

5 Conclusion

In our study in the Golmud–Korla Railway region, we employed numerical simulation to assess the efficacy of the HDPE sheet sand barrier under different wind angles. Our key findings are outlined below:

At a wind speed of 12 m/s, the maximum reductions in wind speed at angles of 30°, 45°, 60°, and 90° between the airflow and the sand barrier are about 40%, 48%, 62%, and 81%, respectively. Notably, as this angle widens, the airflow slows down more, and the downwind low-velocity zone expands.

At angles of 30°, 45°, 60°, and 90° between the airflow and the sand barriers, the windproof efficiency peaks at 37.1%, 43.6%, 60.5%, and 76.2%, respectively. The efficiency escalates with a broader angle. Additionally, on the downwind side, the efficiency first increases with distance from the barriers and subsequently diminishes. When the incoming wind speed remains constant, sand barriers positioned at a 90° angle to the airflow offer the most effective wind protection.

Around the sand barriers, patterns of forward erosion and sedimentation change with varying wind angles. When wind speeds reach 12 m/s, and the angles between the airflow and sand barriers vary (30°, 45°, 60°, 90°), the sedimentation area lengthens correspondingly: 1.5H at 30°, 5.0H at 45°, 9.9H at 45°, and 16.3H at 90°. This pattern indicates that as the angle widens, the sedimentation area increases in length, gradually giving way to the forward erosion area. In essence, a greater angle between airflow and sand barriers extends sand sedimentation ranges, augments sand sedimentation quantities, and bolsters the protective effectiveness of the barriers.

Author Contribution

ZHANG Kai: Conceptualization, Supervision, Funding acquisition, Validation, Writing–review and

editing. ZHANG Pei-li: Data curation, Writing–original draft, Project administration, Visualization, Investigation. ZHANG Hai-long: Supervision, Funding acquisition, Investigation. TIAN Jian-jin: Validation, Visualization. WANG Zheng-hui: Conceptualization, Visualization, Investigation. XIAO Jian-hua: Funding Acquisition, Supervision.

Ethics Declaration

Availability of Data/Materials: Researchers interested in accessing the data can contact the corresponding author.

Conflict of Interest: The authors declare no conflicts of interest.

References

Bruno L, Fransos D, Giudice AL (2018) Solid barriers for windblown sand mitigation: Aerodynamic behavior and conceptual design guidelines. J Wind Eng Ind Aerod 173: 79-90.
https://doi.org/10.1016/j.jweia.2017.12.005

Bruno L, Horvat M, Raffaele L (2018) Windblown sand along railway infrastructures: A review of challenges and mitigation measures. J Wind Eng Ind Aerod 177: 340-365.
https://doi.org/10.1016/j.jweia.2018.04.021

Bruno L, Fransos D (2015) Sand transverse dune aerodynamics: 3D coherent flow structures from a computational study. J Wind Eng Ind Aerod 147: 291-301.
https://doi.org/10.1016/j.jweia.2015.07.014

Bradley EF, Mulhearn PJ (1983) Development of velocity and shear stress distribution in the wake of a porous shelter fence. J Wind Eng Ind Aerod 15(1-3): 145-156.
https://doi.org/10.1016/0167-6105(83)90185-X

Blocken B, Stathopoulos T, Carmeliet J (2007) CFD simulation of the atmospheric boundary layer: wall function problems. Atmos Environ 41(2): 238-252.
https://doi.org/10.1016/j.atmosenv.2006.08.019

Bauer BO, Houser CA, Nickling WG (2004) Analysis of velocity profile measurements from wind-tunnel experiments with saltation. Geomorphology 59(1-4): 81-98.
https://doi.org/10.1016/j.geomorph.2003.09.008

Chen B, Cheng J, Xin L, et al. (2019) Effectiveness of hole plate-type sand barriers in reducing aeolian sediment flux: Evaluation of effect of hole size. Aeolian Res 38: 1-12.
https://doi.org/10.1016/j.aeolia.2019.03.001

Cheng JJ, Lei JQ, Li SY, et al. (2016) Disturbance of the inclined inserting-type sand fence to wind-sand flow fields and its sand control characteristics. Aeolian Res 21: 139-150.
https://doi.org/10.1016/j.aeolia.2016.04.008

Cui XN, Liang KX, Wang QC, et al. (2018) Sand-control mechanism of sand blocking embankment at Golmud-Korla Railway. J Arid Land Resour Environ 33(07): 85-92. (In Chinese)
https://doi.org/10.13448/j.cnki.jalre.2019.202

Dong Z, Qian G, Luo W, et al. (2006) Threshold velocity for wind erosion: the effects of porous fences. Environ Geol 51: 471-475.
https://doi.org/10.1007/s00254-006-0343-9

Ding BS, Gao L, Cheng JJ, et al. (2021) Numerical Simulation of Wind-Sand Flow Characteristics of Inclined Inserting-Type Sand Fence Under Influence of Inserting Plate Angle. Bulletin of Soil and Water Conservation 41(01): 132-137. (In Chinese)
https://doi.org/10.13961/j.cnki.stbctb.2021.01.019

Fryberger SG, Dean G, McKee ED (1979) Dune forms and wind regime. A study of global sand seas 1052: 137-170.

Gillies JA, Etyemezian V, Nikolich G, et al. (2017) Effectiveness of an array of porous fences to reduce sand flux: Oceano Dunes, Oceano CA. J Wind Eng Ind Aerod 168: 247-259.
https://doi.org/10.1016/j.jweia.2017.06.015

Gillies JA, Nickling WG, Nikolich G, et al. (2017) A wind tunnel study of the aerodynamic and sand trapping properties of porous mesh 3-dimensional roughness elements. Aeolian Res 25: 23-35.
https://doi.org/10.1016/j.aeolia.2017.02.001

Guo CY, Han ZW, Zhong S (2017) Wind profile characteristics of new materials sand-barriers in Hobq Desert. Bulletin of Soil and Water Conservation 37: 260-265. (In Chinese)
https://doi.org/10.13961/j.cnki.stbctb.2017.05.044

Hesp PA, Dong Y, Cheng H, et al. (2019) Wind flow and sedimentation in artificial vegetation: Field and wind tunnel experiments. Geomorphology 337: 165-182.
https://doi.org/10.1016/j.geomorph.2019.03.020

Horvat M, Bruno L, Khris S (2021) CWE study of wind flow around railways: Effects of embankment and track system on sand sedimentation. J Wind Eng Ind Aerod 208: 104476.
https://doi.org/10.1016/j.jweia.2020.104476

Horvat M, Bruno L, Khris S (2022) Receiver Sand Mitigation Measures along railways: CWE-based conceptual design and preliminary performance assessment. J Wind Eng Ind Aerod 228: 105109.
https://doi.org/10.1016/j.jweia.2022.105109

Kok JF, Parteli EJ, Michaels TI, et al. (2012) The physics of wind-blown sand and dust. Rep Prog Phys 75(10): 106901.
https://doi.org/10.1088/0034-4885/75/10/106901

Lai JH, Zhang K, Wang WS, et al. (2017) Research advances and prospect in chemical sand-fixing materials. J Desert Res 37(4): 644-658. (In Chinese)
https://doi.org/10.7522/j.issn.1000-694X.2016.00032

Li JR, Guo JY, Dong Z, et al. (2016) Sand moving characteristics and the protective effect of governance measures along bank of Yellow River in Ulan Buh Desert. J Arid Land Resour and Environ 30(08): 113-119. (In Chinese)
https://doi.org/10.13448/j.cnki.jalre.2016.258

Li BL, Sherman DH (2015) Aerodynamics and morphodynamics of sand fences: A review. Aeolian Res 17: 33-48.
https://doi.org/10.1016/j.aeolia.2014.11.005

Lima IA, Parteli EJ, Shao Y, et al. (2020) CFD simulation of the wind field over a terrain with sand fences: Critical spacing for the wind shear velocity. Aeolian Res 43: 100574.
https://doi.org/10.1016/j.aeolia.2020.100574

Li XM, Xin GW, Song YH, et al. (2023) Study on design of mechanical sand prevention measures in different sand damage areas along railway. Railway Investigation and Surveying 49(4): 82-89. (In Chinese)
https://doi.org/10.19630/j.cnki.tdkc.202211260001

Li KC, Zhou Q, Ding LS (2019) Prevention mechanism and effect evaluation of HDPE sand barrier in Gobi area of southern Xinjiang. China Railw Sci 40(3): 10-14. (In Chinese)
https://doi.org/10.3969/j.issn.1001-4632.2019.03.02

Liang KX, Wang QC, Cui XN, et al. (2018) An analysis of protection benefits of different sand-fixing measures at Golmud-Korla Railway. Bull Soil Water Conserv 38(05): 300-306. (In Chinese)
https://doi.org/10.13961/j.cnki.stbctb.2018.05.048

McClure S, Kim JJ, Lee SJ, et al. (2017) Shelter effects of porous multi-scale fractal fences. J Wind Eng Ind Aerod 163: 6-14.
https://doi.org/10.1016/j.jweia.2017.01.007

Nagata T, Nonomura T, Takahashi S, et al. (2016) Investigation on subsonic to supersonic flow around a sphere at low Reynolds number of between 50 and 300 by direct numerical simulation. Phys Fluids 28(5): 28-47.

https://doi.org/10.1063/1.4947244

Parsons DR, Wiggs GF, Walker IJ, et al. (2004) Numerical modelling of airflow over an idealised transverse dune. Environ Modell Softw 19(2): 153-162. https://doi.org/10.1016/S1364-8152(03)00117-8

Qu JJ, Ling YQ, Jing ZF, et al. (2007) Interaction between sand blown activity and protection system in Shapotou section of Baotou-Lanzhou Railway. J Desert Res 27(4): 529-533. (In Chinese)

Qu JJ, Yu WB, Qin XB (2014) Wind-protecting efficiency of HDPE functional sand-fixing barriers. J Desert Res 34(5): 1185-1193. (In Chinese) https://doi.org/10.7522/j.issn.1000-694X.2013.00446

Qi YL (2021) Protection benefits of mechanical sand control measures in Gobi district, southern Xinjianc. J Railw Sci Eng 18(04): 892-900. (In Chinese) https://doi.org/10.19713/j.cnki.43-1423/u.T20200517

Raffaele L, Bruno L (2019) Windblown sand action on civil structures: Definition and probabilistic modeling. Eng Struct 178: 88-101. https://doi.org/10.1016/j.engstruct.2018.10.017

Rosenbrand E, van Beek V, Bezuijen A, et al. (2022) Multi-scale experiments for a coarse sand barrier against backward erosion piping. Géotechnique 72(3): 216-226. https://doi.org/10.1680/jgeot.19.P.358

Raffaele L, Bruno L, Pellerey F, et al. (2016) Windblown sand saltation: a statistical approach to fluid threshold shear velocity. Aeolian Res 23: 79-91. https://doi.org/10.1016/j.aeolia.2016.10.002

Raffaele L, van Beeck J, Bruno L (2021) Wind-sand tunnel testing of surface-mounted obstacles: Similarity requirements and a case study on a sand mitigation measure. J Wind Eng Ind Aerod 214: 104653. https://doi.org/10.1016/j.jweia.2021.104653

Sun QW, Wang T, Han ZW, et al. (2004) Blown sand harm along north Xinjiang railway and its control. J Desert Res 24(2): 182-186. (In Chinese)

Sun H, Liu J, Huang Q (2017) Numerical analysis for force at embedded end of sand barrier under wind loads. Trans Chin Soc Agric Eng 33(2): 148-154. (In Chinese) https://doi.org/10.11975/j.issn.1002-6819.2017.02.020

Sun J, Wang J, Wang H (2023) Wind tunnel test study on windbreak and sand fixing effect of porous sand fixing brick grid mechanical sand barrier. J Vibration and Shock 42(19): 266-274. (In Chinese) https://doi.org/10.13465/j.cnki.jvs.2023.19.034

Tie S, Jiang X, Wang CA (2013) Progress in chemical sand-fixing materials in desertification combating. Sci Technol Rev 31(5/6): 106-111. (In Chinese) https://doi.org/10.3981/j.issn.1000-7857.2013.h1.020

Wang R, Zhou LH, Chen Y (2017) Wind-blown sand control effect of sand barriers used in the Kubq Desert. Arid Zone Res 34(2): 330-336. (In Chinese) https://doi.org/10.13866/j.azr.2017.02.12

Wang YM, Chen WW, Han WF (2005) Microstudy on mechanism of sand fixation with SH. Rock Soil Mech 26(4): 650-654. (In Chinese) https://doi.org/10.16285/j.rsm.2005.04.031

Wang T, Qu J, Ling Y, et al. (2018) Shelter effect efficacy of sand fences: A comparison of systems in a wind tunnel. Aeolian Res 30: 32-40. https://doi.org/10.1016/j.aeolia.2017.11.004

Wang H, Wang H, Gao F, et al. (2018) Literature review on pressure-velocity decoupling algorithms applied to built-environment CFD simulation. Build Environ 143: 671-678. https://doi.org/10.1016/j.buildenv.2018.07.046

Wu XX, Zou XY, Zhang CL, et al. (2013) The effect of wind barriers on airflow in a wind tunnel. J Arid Environ 97: 73-83.

https://doi.org/10.1016/j.jaridenv.2013.05.003

White BR (1996) Laboratory simulation of aeolian sand transport and physical modeling of flow around dunes. Annals of Arid Zone 35: 187-213. T:\Papers\LabSim2.doc\7/25/2000

Xiao HL, Li XR, Song YX, et al. (2004) Impact of evolvement of soil-plant system on engineering of mobile sand dunes control. Sci Silvae Sin 40(1): 24-30. (In Chinese)

Yu YP, Zhang KC, An ZS, et al. (2020) The blocking effect of the sand fences quantified using wind tunnel simulations. J Mt Sci-Engl 17(10): 2485-2496. https://doi.org/10.1007/s11629-020-6095-2

Yan M, Wang H, Zuo H, et al. (2019) Wind tunnel simulation of an opencut tunnel airflow field along the Linhe-Ceke Railway, China. Aeolian Res 39: 66-76. https://doi.org/10.1016/j.aeolia.2019.04.007

Zhang HX (2023) Design of biological control scheme for wind-sand hazard section of Golmud-Korla Railway. Railway Standard Design 67(01): 191-196+202. (In Chinese) https://doi.org/10.13238/j.issn.1004-2954.202112070004

Zhang K, Zhao P, Zhao J, et al. (2021) Protective effect of multi-row HDPE board sand fences: A wind tunnel study. Int Soil Water Conse 9(1): 103-115. https://doi.org/10.1016/j.iswcr.2020.08.006

Zhang K, Yang ZJ, Wang QC, et al. (2019) Relationship between porosity and effective protection distance of HDPE board sand barrier on Golmud-Korla Railway. J China Railw Sci 40(5): 16-21. (In Chinese) https://doi.org/10.3969/j.issn.1101-4632.2019.05.03

Zhang K, Wang QC, Yang ZJ, et al. (2019) Research on numerical simulation on wind protection benefits of HDPE panels with high vertical sand barrier in the newly-built Golmud-Korla Railway. J China Railw Soc 41(3): 169-175. (In Chinese) https://doi.org/10.3969/j.issn.101-8360.2019.03.023

Zhang XX, Zhang K, Shi BY, et al. (2021) Numerical simulation of wind-blown sand flow field and formation mechanismof sand damage on road surface in shifting dune area. Arid Zone Res 38(04): 1184-1191. (In Chinese) https://doi.org/10.13866/j.azr.2021.04.30

Zhang K, Zhang HL, Deng YH, et al. (2023) Effects of sand sedimentation and wind erosion around sand barrier: Numerical simulation and wind tunnel test studies. J Mt Sci-Engl 20(4) 962-978. https://doi.org/10.1007/s11629-022-7757-z

Zhang K, Zhao PW, Zhang XX, et al. (2020) Study on difference of wind-sand flow of HDPE board high vertical sand fence by wind velocity profile. J China Railw Soc 42(9): 143-149. (In Chinese) https://doi.org/10.3969/j.issn.1001-8360.2020.09.018

Zhang K, Wang QC, Zhang XX, et al. (2020) Effective protection distance of HDPE board fence in Golmud-Korla Railway. J Traffic Transp Eng 20(5): 105-115. (In Chinese) https://doi.org/10.19818/j.cnki.1671-1637.2020.05.008

Zhang K, Tian J, Qu J, et al. (2022) Sheltering effect of punched steel plate sand fences for controlling blown sand hazards along the Golmud-Korla Railway: Field observation and numerical simulation studies. Journal of Arid Land 14(6): 604-619. https://doi.org/10.1007/s40333-022-0019-7

Zhang X, Xie S, Pang Y (2023) Numerical simulation on wind-sand flow field around railway embankment with different wind angles. Front Env Sci-Switz 10: 1073257. https://doi.org/10.3389/fenvs.2022.1073257

Zhang Z, Dong Z, Qian G (2017) Field observations of the vertical distribution of sand transport characteristics over fine, medium and coarse sand surfaces. Earth Surf Proc Land 42(6): 889-902. https://doi.org/10.1002/esp.4045